


Article

Adsorption Tuning of Polarity and Magnetism in AgCr_2S_4 Monolayer

Ranran Li, Yu Wang, Ning Ding, Shuai Dong  and Ming An *

School of Physics, Southeast University, Nanjing 211189, China

* Correspondence: sdong@seu.edu.cn (S.D.); amorn@seu.edu.cn (M.A.)

Abstract: As a recent successfully exfoliated non-van der Waals layered material, AgCrS_2 has received a lot of attention. Motivated by its structure-related magnetic and ferroelectric behavior, a theoretical study on its exfoliated monolayer AgCr_2S_4 has been carried out in the present work. Based on density functional theory, the ground state and magnetic order of monolayer AgCr_2S_4 have been determined. The centrosymmetry emerges upon two-dimensional confinement and thus eliminates the bulk polarity. Moreover, two-dimensional ferromagnetism appears in the CrS_2 layer of AgCr_2S_4 and can persist up to room temperature. The surface adsorption has also been taken into consideration, which shows a nonmonotonic effect on the ionic conductivity through ion displacement of the interlayer Ag, but has little impact on the layered magnetic structure.

Keywords: AgCr_2S_4 ; two-dimensional materials; magnetism; polarity

1. Introduction

Recently, a large number of new two-dimensional (2D) functional materials have been synthesized and reported, including those with intrinsic ferroelectric and long-range spin orders, which have greatly stimulated people's research enthusiasm for 2D ferroic materials [1–12].

Inspired by graphene, most previous research has focused on 2D layered van der Waals (vdW) materials, whose atomic-thin layers can be easily obtained by mechanical exfoliation due to their weak vdW interlayer bonding [13–15]. With the development of 2D research, more feasible approaches emerge. As a supplement to mechanical cleavage, those methods can artificially open a gap between layers of non-vdW materials through selective etching or ionic intercalation. The 2D layer can then be obtained through post-procedure. The typical representatives prepared by chemical etching and intercalation are MXene and AM_2X_4 , respectively [16,17]. Since then, non-vdW layered materials soon became another emerging branch of 2D materials, especially those with intrinsic ferroelectricity, long-range spin orders, or both. For example, NaCrX_2 with adjustable conductivity and ACr_2S_4 ($A = \text{Li}, \text{Na}, \text{K}, \text{Rb}$) nanosheets with multiferroic properties have been reported recently [18,19].

AgCrS_2 is one such layered material with both long-range magnetic order and ferroelectricity. This compound was synthesized in 1957 [20]. It is composed of an alternative stacking of edge-sharing octahedra CrS_2 layers and Ag ion layers along the c -axis in a trigonal lattice ($R3m$) around room temperature. When cooled down to T_N (about 40 K), the lattice changes to monoclinic (Cm), accompanied by the emergence of in-plane double stripes (DS) antiferromagnetic (AFM) order [21,22]. The ferroelectricity originates from the off-centering displacement of Ag ions. Several experimental works found that this polarization is closely related to the structural and magnetic transition [21,22]. Recently, the monolayer AgCr_2S_4 , consisting of a single Ag layer sandwiched between two CrS_2 layers, was successfully exfoliated from AgCrS_2 bulk [17]. Interest has been aroused [23,24], mainly focusing on the magnetic and ferroelectric properties of single-layer AgCr_2S_4 . However, the specific structure of the monolayer, the possible surface adsorption after peeling, and their effects on material properties have not been well explored.



Citation: Li, R.; Wang, Y.; Ding, N.; Dong, S.; An, M. Adsorption Tuning of Polarity and Magnetism in AgCr_2S_4 Monolayer. *Materials* **2023**, *16*, 3058. <https://doi.org/10.3390/ma16083058>

Academic Editor: George Kioseoglou

Received: 1 March 2023

Revised: 3 April 2023

Accepted: 11 April 2023

Published: 12 April 2023



Copyright: © 2023 by the authors. Licensee MDPI, Basel, Switzerland. This article is an open access article distributed under the terms and conditions of the Creative Commons Attribution (CC BY) license (<https://creativecommons.org/licenses/by/4.0/>).

In this work, based on density functional theory (DFT), the magnetic ground state of bulk AgCrS_2 has been checked. Our calculation results on bulk are consistent with recent experimental observations, which not only ensure the feasibility of our calculation but also form a solid basis for the following study on its monolayer. The structural, magnetic, and electronic properties of AgCr_2S_4 monolayer have been further studied. Unexpectedly, the polar symmetry inherited from the parent phase could not be preserved during optimization. Moreover, ferromagnetic (FM) order appears in the in-plane Cr triangular lattice with relatively weak interplane AFM coupling. The situation changes when hydrogen adsorption is taken into consideration. After adsorption, the intralayer FM and interlayer AFM ground state remains unchanged, but the structural symmetry is altered along with its ferroelectricity and ionic transport behavior.

2. Methods

Our DFT calculations were performed using Vienna ab initio Simulation Package (VASP) [25,26]. The electronic interactions were described by projector-augmented-wave (PAW) pseudo-potentials, with semicore states treated as valence states [27]. The exchange and correlation were treated using Perdew–Burke–Ernzerhof (PBE) parametrization of the generalized gradient approximation (GGA) [28]. To properly describe the correlated electrons, the GGA+ U method was adopted, and the on-site Hubbard U_{eff} was imposed on Cr's 3d orbitals using the Dudarev approach for all calculations [29]. The plane-wave cutoff energy was set to 500 eV. The Monkhorst–Pack K -point meshes were chosen as $2 \times 8 \times 4$ and $7 \times 7 \times 1$ for bulk and monolayer calculations, respectively. Exchange coefficients and magnetic ground states for the monolayer were estimated based on a $2 \times 4 \times 1$ supercell with various magnetic orders. The convergent criterion for the energy was set to 10^{-5} eV, and that of the Hellman–Feynman forces during structural relaxation was 0.01 eV/Å.

In the study of the monolayer structure, a vacuum layer of 20 Å was added along the c -axis direction to avoid the interaction between two neighboring slices. The possible switching paths between different structure phases were evaluated by the nudged elastic band (NEB) method [30]. To estimate the Curie temperature and the temperature evolution of magnetic properties, the Markov-chain Monte Carlo (MC) method with Metropolis algorithm was employed to simulate the magnetic ordering [31]. The MC simulation was performed on a 40×40 lattice with periodic boundary conditions, and larger lattices were also tested to confirm the physical results. The simulations were performed with 20,000 equilibration steps and 80,000 averaging steps. All MC simulations are gradually cooled down from the initial disordered state at high temperature to the low temperature under investigation.

3. Results

3.1. AgCrS_2 Bulk Properties

As mentioned above, the low-temperature bulk crystal belongs to the Cm space group without spatial inversion symmetry. Its intrinsic layered feature is illustrated in Figure 1a. The Cr^{3+} ions located at the center of CrS_6 octahedra form a triangular magnetic lattice within each CrS_2 layer. Recently, an in-plane collinear magnetic structure has been reported, showing DS pattern (as shown in Figure 1c) with AFM coupling in between [22,32]. The magnetic ordering and structural transition occur simultaneously, accompanied by the emergence of ferroelectricity, indicating the strong connection between magnetic, ferroelectric, and structural properties [32–35].

To determine the magnetic ground state, three common collinear configurations on the triangular lattice, as depicted in Figure 1c, have been taken into account in addition to the reported DS order. Besides, in order to study the interlayer magnetic coupling, the intralayer FM and interlayer AFM (A-AFM) configuration has also been considered. Our calculation results show that the DS-AFM pattern is indeed the magnetic ground state when U_{eff} is less than 0.8 eV (Figure 1d). The total energy of AFM zigzag and stripe configurations are always higher than that of DS-AFM and are almost insensitive to the U_{eff}

value. In contrast, the energy of A-AFM and FM decrease with increasing U_{eff} , showing a similar trend. The A-AFM order is energetically more favorable than FM, and will even replace DS-AFM as the ground state when U_{eff} is larger than 0.8 eV. Obviously, a specific U_{eff} value (i.e., 0.6 eV) is vital in precisely reproducing AgCrS_2 bulk properties. The local magnetic moment increases with the increase in U_{eff} , reaching $2.86 \mu_{\text{B}}/\text{Cr}$ at 0.6 eV, which is consistent with previously reported value [22]. Moreover, the optimized lattice constants ($a = 13.83 \text{ \AA}$, $b = 3.54 \text{ \AA}$, and $c = 7.13 \text{ \AA}$) are in good agreement with the experimental data [22,24]. Therefore, it will be adopted in the following calculations by default.

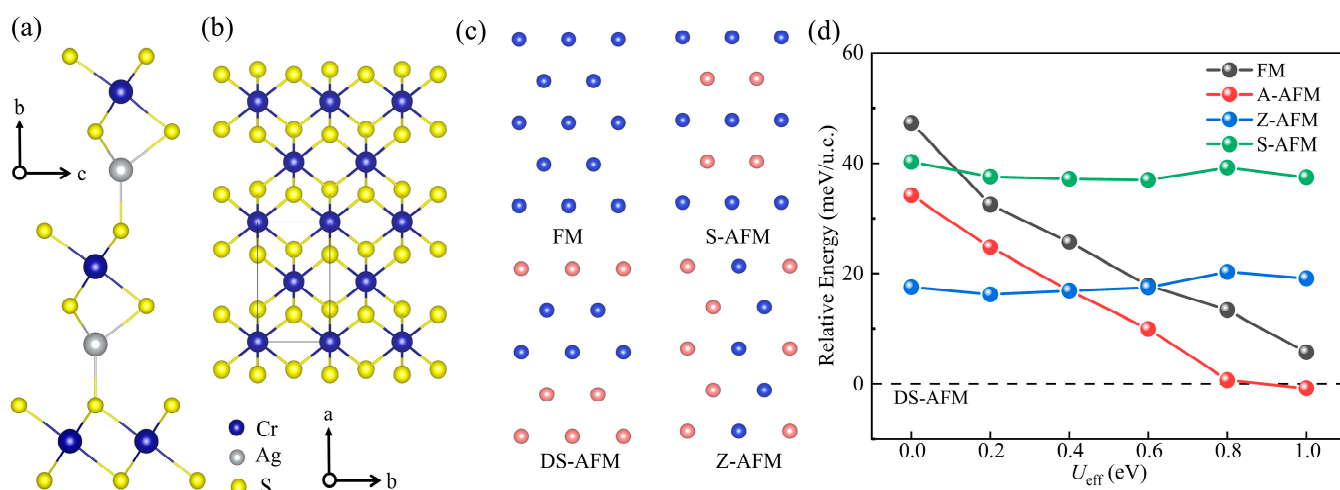


Figure 1. (a,b) Side view and top view of bulk AgCrS_2 . (c) Four in-plane magnetic configurations: ferromagnetic order (FM), stripe AFM (S-AFM), double-stripe order (DS-AFM), and zigzag AFM order (Z-AFM). Blue and red spheres indicate spin-up and spin-down Cr ions, respectively. The other ions are omitted for clarity. (d) The energy evolution of various magnetic orders as a function of U_{eff} . The DS state energy is taken as the reference value.

3.2. AgCr_2S_4 Monolayer

Recently, AgCrS_2 was successfully exfoliated into 2D nanosheets by Peng et al. through ion intercalation [17]. These 2D sheets can be thinned down to a monolayer containing one Ag ion layer sandwiched between two CrS_2 layers. As can be seen from Figure 2a,b, the edge-sharing octahedral framework is inherited in CrS_2 layers, while the relative displacement of the center Ag ion will give rise to two distinct structural phases (i.e., the asymmetric α phase and the centrosymmetric β phase). The detailed structural information is shown in Table S1 and Figure S1. In the following, we will focus on the structural, magnetic, and electronic properties of AgCr_2S_4 monolayer.

To find the ground state of AgCr_2S_4 monolayer, the total energies of different magnetic orders mentioned earlier have been calculated based on the above two structural phases. The calculation results have been summarized in Table 1. Obviously, the energy of the β phase is always lower than that of the α phase, presenting a clear tendency to restore the central symmetry of the 2D single layer, contrary to its parent bulk phase.

Table 1. The energy differences of four in-plane collinear spin configurations. Interlayer coupling has also been considered, in which the AFM interlayer coupling is denoted by subscript 1 and the FM coupling is represented by subscript 2, respectively. The total energy of the ground state (β phase with A-AFM order) is taken as the reference value, in units of meV/Cr.

	A-AFM	DS ₁ -AFM	Z ₁ -AFM	S ₁ -AFM	FM	DS ₂ -AFM	Z ₂ -AFM	S ₂ -AFM
α	57.25	68.40	82.62	88.25	53.65	66.44	82.82	23.39
β	0	14.99	11.69	24.00	2.88	13.67	13.40	22.41

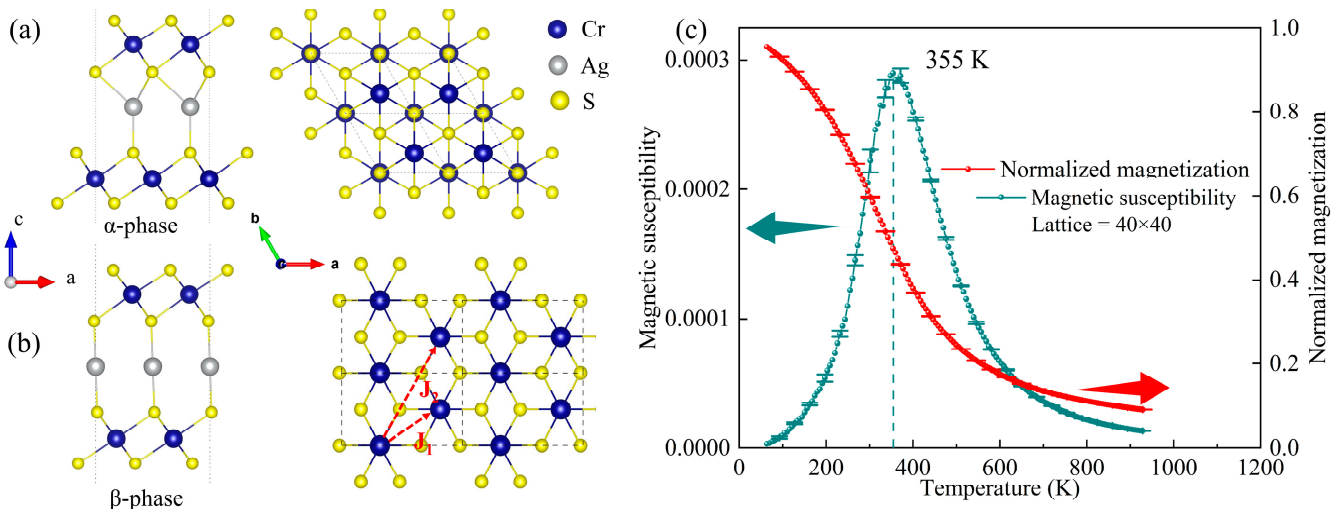


Figure 2. (a,b) The top and side views of the AgCr_2S_4 asymmetric α phase (P3m1) and the centrosymmetric β phase (C2/m), respectively. The nearest neighbor interaction J_1 and the next-nearest neighbor interaction J_2 are denoted by the red dotted arrows in the right panel of (b). (c) The MC simulated magnetic susceptibility and normalized magnetization as a function of temperature for the AgCr_2S_4 monolayer.

Our results also indicate that the magnetic Cr ions in each CrS_2 layer tend to couple ferromagnetically and show no sensitivity to the above two structural phases. This structure-insensitive FM behavior, in contrast with its bulk form, can be reasonably interpreted on the basis of the d orbital occupation of Cr. In the AgCrS_2 bulk, Cr^{3+} ion is in the $3d^3$ configuration. According to the Goodenough–Kanamori–Anderson (GKA) rules [36–38], the half-filled t_{2g} orbitals give rise to AFM direct exchange, while the p orbital intermediated Cr–S–Cr super exchange favors FM coupling. It is the competing exchange interactions that make the bulk magnetic order structurally related. In contrast, from the change of chemical formula before and after exfoliation, the Cr ion in AgCr_2S_4 monolayer is in the mixed valence state (Cr_2^{7+}). The hole hopping between neighboring Cr’s d orbitals gives rise to the strong FM tendency and is insensitive to structural details.

To characterize this in-plane triangular magnetic lattice, the classical Heisenberg spin model is adopted, which can be constructed as

$$H = J_1 \sum_{\langle i,j \rangle} S_i \cdot S_j + J_2 \sum_{[i,k]} S_i \cdot S_k + \sum_i [K_c (S_i^z)^2 + K_b (S_i^y)^2]$$

where S_i is the normalized spin ($|S| = 1$) on the Cr site i . J_1 and J_2 correspond to the in-plane exchange constants between the nearest-neighbor (NN) and the next-nearest-neighbor (NNN) interactions, as labeled in Figure 2b, respectively. $K_{b/c}$ stands for the single-ion magnetocrystalline anisotropy along the b -/ c -axis, respectively. Based on the ground structure (β phase), these exchange coefficients can be extracted by comparing DFT energy with different spin orders. Specifically, in a $2 \times 4 \times 1$ supercell, the energy of these magnetic states can be expressed as

$$\begin{aligned} E_{\text{FM}} &= E_0 + 3J_1 + 3J_2 \\ E_{\text{DS}} &= E_0 + J_1 - J_2 \\ E_{\text{Z}} &= E_0 - J_1 + J_2 \end{aligned}$$

where E_0 is the nonmagnetic energy. The derived parameters are summarized in Table 2. According to our estimation, the NN exchange interactions are FM and dominated, as expected from our previous analysis. The NNN exchange constant J_2 is relatively weak due to its indirect and long-distance bonding. Based on these exchange parameters, MC

simulations were employed to determine the Curie temperature. Additionally, the magnetic susceptibility was calculated. The system reaches equilibrium at a given temperature, the magnetization M and magnetic susceptibility χ are calculated as [39]

$$M = \frac{1}{N} \sum_{i=1}^N S_i$$

$$\chi = \frac{\langle M^2 \rangle - \langle M \rangle^2}{k_B T}$$

where N represents the total number of spin sites. Given the exact solution of the spin Hamiltonian, T_C can be estimated from the peak position of the specific magnetic susceptibility χ (or the maximum slope point of magnetization M). MC results are shown in Figure 2c, indicating that the magnetic transition temperature is above room temperature, much higher than its parent bulk, as expected from its changed and mixed valence of Cr ions. Our MC simulation have also been tested on multi-size lattices to exclude the finite size effect. As shown in Figure S2, the magnetization and susceptibility curve are not sensitive to lattice size, and the Curie temperature shows no obvious scale effect.

Table 2. In-plane exchange parameters (meV/Cr) estimated from our DFT calculations.

	J_1	J_2	K_b	K_c
β phase	−14.86	−5.76	1.11	0.80

Since the AgCr_2S_4 monolayer contains two CrS_2 layers, the interlayer coupling has also been considered. Our calculation shows that the interlayer AFM coupling is energetically more favorable than FM coupling, although the energy difference is quite limited (within 3 meV). After exfoliation, the CrS_2 - CrS_2 interlayer coupling decreases with the increase in the interlayer spacing (from 4.60 Å to 4.76 Å), which is consistent with the intuition. These weakly coupled 2D FM triangular lattices in the AgCr_2S_4 monolayer may provide a new approach for magnetic regulation in spintronic devices.

The electronic densities of states (DOS) of AgCrS_2 bulk and AgCr_2S_4 monolayer are shown in Figure 3. The parent bulk phase exhibits insulating characteristics with a moderate gap of about 1.5 eV. The states near the Fermi level mainly originate from Cr's 3d orbitals. In the AgCr_2S_4 monolayer, the stripping induced hole-doping causes a negative shift in the Fermi level, and therefore closes the gap. Meanwhile, Cr's dominant contribution to the Fermi level is not affected upon peeling.

In addition, we also verified the mechanical stability of AgCr_2S_4 . The in-plane elastic constants and various mechanical parameters are summarized in Tables S2 and S3, respectively. Our calculation results prove that AgCr_2S_4 is a soft and malleable material, similar to its three-dimensional counterpart [40]. The schematic diagrams of Young's modulus, shear modulus, and Poisson's ratio are given in Figure S5.

3.3. H Adsorption Effect

The AgCr_2S_4 monolayer is synthesized through wet chemical exfoliation of bulk AgCrS_2 . Analogous to MXene, the high surface area to volume ratio and the unsaturated bonds of the outer layer sulfur ions may lead to the adsorption of ions at surface sites during preparation. Thus, the hydrogen adsorption and its effect on structural and magnetic properties of AgCr_2S_4 monolayer have been investigated. First, the unilateral passivation is considered. As labeled in Figure 4a,b, there are ten possible adsorption sites. According to our calculations, the energetically most favorable adsorption site (denoted as C in Figure 4a) is located right above the sulfur anion. Detailed adsorption sites and adsorption energy are provided in the supplementary material. After unilateral hydrogen passivation, the central Ag layer shifts away from the adsorption side due to electrostatic repulsion, recovering the original bulk-like AgS_4 tetrahedron with neighboring S ions.

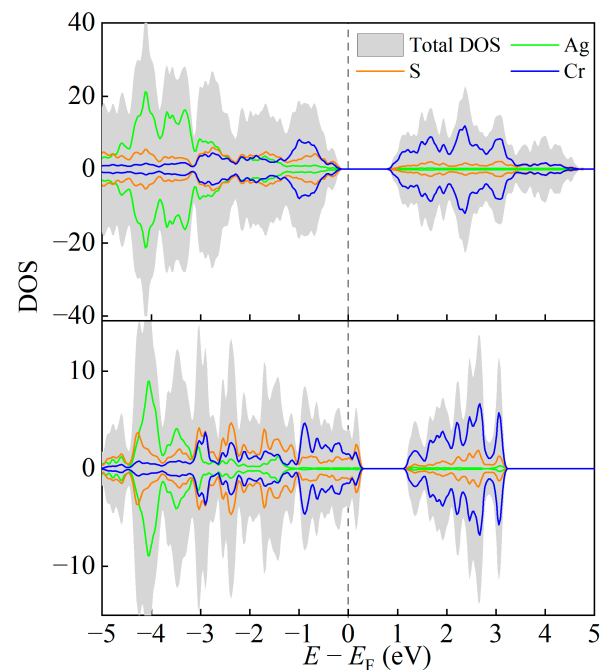


Figure 3. The density of states (DOS) of bulk AgCrS_2 (upper panel) and monolayer AgCr_2S_4 (lower panel).

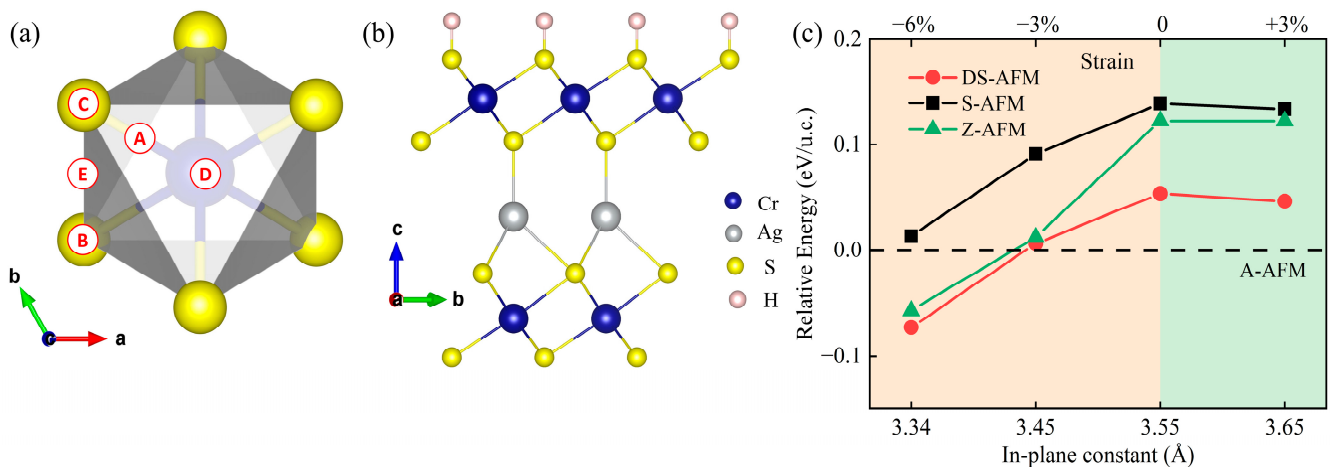


Figure 4. (a) Possible adsorption sites for hydrogen. B, C, D denote the adsorption sites above the lower and upper S ions and Cr ion in the adjacent CrS_2 layer, respectively. While, A and E are the adsorption sites located between CD and BC, respectively. (b) Side view of the ground structure of unilaterally passivated $\text{AgCr}_2\text{S}_4\text{H}$. (c) $\text{AgCr}_2\text{S}_4\text{H}$ ground state phase diagram as a function of the lattice constant. Relative energy per unit cell is shown on the left axis. The energy of optimized free-standing structure with A-AFM ground state is taken for reference. Upper axis: the equivalent biaxial strain, defined as $(a - a_0)/a_0$, where a_0 and a are the in-plane lattice constants before and after stress application, respectively.

Nonetheless, the magnetic ground state of $\text{AgCr}_2\text{S}_4\text{H}$ remains A-AFM (e.g., in-plane FM). It is nontrivial, since the chemical valence of Cr has been restored to its bulk value (i.e., +3) after the hydrogen adsorption. The in-plane DS-AFM order observed in bulk has not been recovered, which is a little bit unexpected. As discussed previously, the in-plane magnetic pattern in bulk is structurally related, namely the Cr^{3+} ion spacing [22,35]. We compared the in-plane Cr-Cr spacing after unilateral H passivation with that of the bulk material. The Cr-Cr spacing after passivation is 3.55 Å larger than the bulk value (3.43/3.54 Å, this non-uniform spacing distribution is due to the DS-AFM order). According

to GKA rules, the half-filled t_{2g} orbitals of Cr^{3+} give rise to the AFM direct exchange which is sensitive to Cr-Cr spacing. In other words, large spacing weakens this AFM direct exchange, breaks the delicate balance and leads to the FM dominance, which well explains the FM behavior observed in the passivated $\text{AgCr}_2\text{S}_4\text{H}$ material. Details of lattice constants are marked in Figure S4. This speculation is further proved by in-plane strain modulation. As shown in Figure 4c, the in-plane magnetic ground state is fragile and extremely sensitive to biaxial strain. The compressive strains can effectively shorten the in-plane Cr-Cr distance and enhance the direct AFM coupling, thus giving rise to the bulk-like DS order. On the contrary, the tensile strains will fasten the in-plane FM order (i.e., A-AFM).

In AgCrS_2 bulk, the sandwiched Ag layer has been proved to be crucial to its structure, ferroelectricity, and ionic conductivity [17,20,33]. Here, in AgCr_2S_4 monolayer, Ag's displacement to the central site restores the centrosymmetry and destroys the ferroelectricity. This displacement not only increases the CrS_2 interlayer distance, but also weakens the binding between Ag ion and the upper/lower CrS_2 layers (Ag-S bonds are halved from 4 to 2), which will certainly lead to the enhancement of ionic mobility as found in experiment [20].

To confirm this scenario, the possible displacement processes of Ag ion in AgCr_2S_4 as well as its H-passivated cases are simulated by the NEB method. The corresponding energy profiles are shown in Figure 5. Obviously, unilateral adsorption breaks the centro-symmetry and forces Ag to shift away from H, resulting in an asymmetric potential profile, which is consistent with our previous analysis. The simulation results of the AgCr_2S_4 monolayer and the bilaterally adsorbed $\text{AgCr}_2\text{S}_4\text{H}_2$ are also presented in Figure 5 for comparison. In both AgCr_2S_2 and $\text{AgCr}_2\text{S}_4\text{H}_2$, the sandwiched Ag ion tends to be located in the central site, with weak bonding between neighboring S ions. The energy barriers of AgCr_2S_2 and $\text{AgCr}_2\text{S}_4\text{H}_2$ are 150 meV/Ag and 140 meV/Ag, respectively, making them much lower than in the case of $\text{AgCr}_2\text{S}_4\text{H}$ (190 meV/Ag). For comparison, the energy barrier of AgCrS_2 bulk was estimated to be 450 meV/Ag [17].

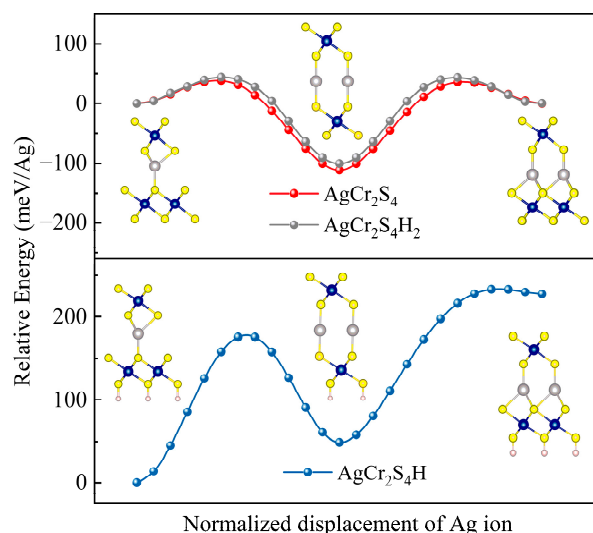


Figure 5. The switching paths of $\text{AgCr}_2\text{S}_4\text{H}_2$ (grey), $\text{AgCr}_2\text{S}_4\text{H}$ (blue), and AgCr_2S_4 (red) as simulated by NEB. Ag, Cr, S, and H ions are represented by gray, dark blue, yellow, and white balls in the illustrations, respectively.

Based on the above analysis and numerical data, it is reasonable to conclude that the ionic conductivity of AgCrS_2 can benefit from dimension reduction and may reach its peak in single-layer AgCr_2S_4 or its $\text{AgCr}_2\text{S}_4\text{H}_2$.

4. Conclusions

In summary, the structural, magnetic, and electronic properties of bulk AgCrS_2 and its single layer AgCr_2S_4 have been investigated. The in-plane DS pattern of bulk material has

been confirmed, but its monolayer exhibits metallic in-plane FM behavior. The underlying mechanism is attributed to the hole-doping induced by exfoliation and the resulting change in Cr's chemical valence. Moreover, the displacement of the sandwiched Ag ion towards the high-symmetry center was found, which eliminates the polarity and enhances the ionic conductivity. This structure-related superionic behavior is sensitive to surface adsorption. Specifically, it will be inhibited by unilateral adsorption, but will be recovered by bilateral adsorption. The present study may stimulate further experimental and theoretical research on AgCr_2S_4 and other 2D non-vdW materials.

Supplementary Materials: The following supporting information can be downloaded at: <https://www.mdpi.com/article/10.3390/ma16083058/s1>, Figure S1: In-plane structural parameters of phases α and β ; Figure S2: MC simulations of the magnetic susceptibility and normalized magnetization of AgCr_2S_4 monolayer at different lattice sizes as a function of temperature; Figure S3: Hydrogen adsorption energy and possible adsorption sites of $\text{AgCr}_2\text{S}_4\text{H}$; Figure S4: Distance between the Cr-Cr of AgCrS_2 and $\text{AgCr}_2\text{S}_4\text{H}$; Figure S5: Young's modulus, shear modulus and Poisson's ratio of AgCr_2S_4 ; Table S1: The lattice constants of AgCr_2S_4 ; Table S2: The elastic constants of AgCr_2S_4 ; Table S3: Mechanical parameters of AgCr_2S_4 ; Table S4: The energy of $\text{AgCr}_2\text{S}_4\text{H}_2$ in different magnetic sequences [40–45].

Author Contributions: Conceptualization, S.D.; methodology, R.L., Y.W. and N.D.; validation, M.A. and S.D.; formal analysis, R.L., Y.W. and N.D.; resources, S.D. and M.A.; writing—original draft preparation, R.L.; writing—review and editing, M.A. and S.D.; visualization, R.L. and Y.W.; supervision, M.A., S.D. and N.D.; project administration, M.A. and S.D. All authors have read and agreed to the published version of the manuscript.

Funding: This research was funded by the National Science Foundation of China (Grant No. 12274069, 12274070).

Informed Consent Statement: Not applicable.

Data Availability Statement: Data supporting these findings are available from the corresponding authors upon request.

Acknowledgments: We thank the Big Data Center of Southeast University for providing the facility support on the numerical calculations.

Conflicts of Interest: The authors declare no conflict of interest.

Abbreviations

U_{eff}	Effective Hubbard parameter. In order to deal with the strong correlation of Cr^{3+} , the Hubbard empirical parameter U is added using Dudarev's approach, $U_{\text{eff}} = U - J$, where U and J are the on-site Coulomb interaction and the strength of the effective on-site exchange interaction, respectively.
S_i	The normalized spin vector sitting on lattice site i .
J_1 and J_2	The in-plane nearest neighbor and the next-nearest neighbor magnetic exchange coupling parameters.
k_B	The Boltzmann constant.
M	The normalized magnetization.
χ	The magnetic susceptibility.

References

- Huang, B.; Clark, G.; Navarro-Moratalla, E.; Klein, D.R.; Cheng, R.; Seyler, K.L.; Zhong, D.; Schmidgall, E.; McGuire, M.A.; Cobden, D.H.; et al. Layer-dependent ferromagnetism in a van der Waals crystal down to the monolayer limit. *Nature* **2017**, *546*, 270–273. [CrossRef] [PubMed]
- Gong, C.; Li, L.; Li, Z.; Ji, H.; Stern, A.; Xia, Y.; Cao, T.; Bao, W.; Wang, C.; Wang, Y.; et al. Discovery of intrinsic ferromagnetism in two-dimensional van der Waals crystals. *Nature* **2017**, *546*, 265–269. [CrossRef] [PubMed]
- Ding, W.; Zhu, J.; Wang, Z.; Gao, Y.; Xiao, D.; Gu, Y.; Zhang, Z.; Zhu, W. Prediction of intrinsic two-dimensional ferroelectrics in In_2Se_3 and other $\text{III}_2\text{-VI}_3$ van der Waals materials. *Nat. Commun.* **2017**, *8*, 14956. [CrossRef] [PubMed]

4. Liu, F.; You, L.; Seyler, K.L.; Li, X.; Yu, P.; Lin, J.; Wang, X.; Zhou, J.; Wang, H.; He, H.; et al. Room-temperature ferroelectricity in CuInP_2S_6 ultrathin flakes. *Nat. Commun.* **2016**, *7*, 12357. [[CrossRef](#)]
5. Chang, K.; Liu, J.W.; Lin, H.C.; Wang, N.; Zhao, K.; Zhang, A.M.; Jin, F.; Zhong, Y.; Hu, X.P.; Duan, W.H.; et al. Discovery of robust in-plane ferroelectricity in atomic-thick SnTe. *Science* **2016**, *353*, 274–278. [[CrossRef](#)]
6. Lee, J.U.; Lee, S.; Ryoo, J.H.; Kang, S.; Kim, T.Y.; Kim, P.; Park, C.H.; Park, J.G.; Cheong, H. Ising type magnetic ordering in ordering thin FePS_3 . *Nano Lett.* **2016**, *16*, 7433–7438. [[CrossRef](#)]
7. Wang, C.; You, L.; Cobden, D.; Wang, J. Towards two-dimensional van der Waals ferroelectrics. *Nat. Mater.* **2023**. [[CrossRef](#)]
8. Dong, S.; Liu, J.-M.; Cheong, S.-W.; Ren, Z. Multiferroic materials and magnetoelectric physics: Symmetry, entanglement, excitation, and topology. *Adv. Phys.* **2015**, *64*, 519–626. [[CrossRef](#)]
9. Shao, Z.; Liang, J.; Cui, Q.; Chshiev, M.; Fert, A.; Zhou, T.; Yang, H. Multiferroic materials based on transition-metal dichalcogenides: Potential platform for reversible control of Dzyaloshinskii-Moriya interaction and skyrmion via electric field. *Phys. Rev. B* **2022**, *105*, 174404. [[CrossRef](#)]
10. Wang, J.; Neaton, J.B.; Zheng, H.; Nagarajan, V.; Ogale, S.B.; Liu, B.; Viehland, D.; Vaithyanathan, V.; Schlom, D.G.; Waghmare, U.V.; et al. Epitaxial BiFeO_3 multiferroic thin film heterostructures. *Science* **2003**, *299*, 1719–1722. [[CrossRef](#)]
11. Khan, K.; Tareen, A.K.; Aslam, M.; Wang, R.; Zhang, Y.; Mahmood, A.; Ouyang, Z.; Zhang, H.; Guo, Z. Recent developments in emerging two-dimensional materials and their applications. *J. Mater. Chem. C* **2020**, *8*, 387–440. [[CrossRef](#)]
12. An, M.; Zhang, Y.; Chen, J.; Zhang, H.-M.; Guo, Y.; Dong, S. Tuning magnetism in layered magnet VI_3 : A theoretical study. *J. Phys. Chem. C* **2019**, *123*, 30545–30550. [[CrossRef](#)]
13. Watanabe, K.; Taniguchi, T.; Kanda, H. Direct-bandgap properties and evidence for ultraviolet lasing of hexagonal boron nitride single crystal. *Nat. Mater.* **2004**, *3*, 404–409. [[CrossRef](#)] [[PubMed](#)]
14. Meric, I.; Dean, C.R.; Petrone, N.; Wang, L.; Hone, J.; Kim, P.; Shepard, K.L. Graphene field-effect transistors based on Boron-Nitride dielectrics. *Proc. IEEE* **2013**, *101*, 1609–1619. [[CrossRef](#)]
15. Shirodkar, S.N.; Waghmare, U.V. Emergence of ferroelectricity at a metal-semiconductor transition in a 1T monolayer of MoS_2 . *Phys. Rev. Lett.* **2014**, *112*, 157601. [[CrossRef](#)]
16. Naguib, M.; Mochalin, V.N.; Barsoum, M.W.; Gogotsi, Y. 25th anniversary article: MXenes: A new family of two-dimensional materials. *Adv. Mater.* **2014**, *26*, 992–1005. [[CrossRef](#)]
17. Peng, J.; Liu, Y.; Lv, H.; Li, Y.; Lin, Y.; Su, Y.; Wu, J.; Liu, H.; Guo, Y.; Zhuo, Z.; et al. Stoichiometric two-dimensional non-van der Waals AgCrS_2 with superionic behaviour at room temperature. *Nat. Chem.* **2021**, *13*, 1235–1240. [[CrossRef](#)]
18. Liu, J.; Wang, Y.; Wang, L.-Y.; Yao, Q.; Huang, C.-C.; Huang, H.-Y.; Li, D.-F. Several promising non-vdW multiferroic half-metallic nanosheets ACr_2S_4 (A = Li, Na, K, Rb): The first-principles researches. *Eur. Phys. J. Plus.* **2023**, *138*, 224. [[CrossRef](#)]
19. Huang, J.; Shi, B.; Pan, F.; Wang, J.; Liu, J.; Xu, D.; Zhang, H.; Xia, T.; Cheng, P. Anisotropic magnetic properties and tunable conductivity in two-dimensional layered NaCrX_2 (X = Te, Se, S) single crystals. *Phys. Rev. Mater.* **2022**, *6*, 094013. [[CrossRef](#)]
20. Hahn, H.; Lorent, C.D. Über ternäre chalkogenide des chroms mit einwertigem kupfer und silber. *Z. Anorg. Allg. Chem.* **1957**, *290*, 68–81. [[CrossRef](#)]
21. Singh, K.; Maignan, A.; Martin, C.; Simon, C. AgCrS_2 : A spin driven ferroelectric. *Chem. Mater.* **2009**, *21*, 5007–5009. [[CrossRef](#)]
22. Damay, F.; Martin, C.; Hardy, V.; André, G.; Petit, S.; Maignan, A. Magnetoelastic coupling and unconventional magnetic ordering in the multiferroic triangular lattice AgCrS_2 . *Phys. Rev. B* **2011**, *83*, 184413. [[CrossRef](#)]
23. Li, M.; Liu, Y.; Dai, Y.; Liu, G.; Zhang, X. A ferromagnetic hybrid Weyl semimetal in two dimensions: The monolayer AgCrS_2 . *J. Mater. Sci.* **2022**, *58*, 281–290. [[CrossRef](#)]
24. Zhao, Y.; Liu, Q.; Zhang, F.; Jiang, X.; Gao, W.; Zhao, J. Multiferroicity in a two-dimensional non-van der Waals crystal of AgCr_2X_4 (X = S or Se). *J. Phys. Chem. Lett.* **2022**, *13*, 11346–11353. [[CrossRef](#)]
25. Kresse, G.; Furthmüller, J. Efficient iterative schemes for ab initio total-energy calculations using a plane-wave basis set. *Phys. Rev. B* **1996**, *54*, 11169–11186. [[CrossRef](#)]
26. Kresse, G.; Furthmüller, J. Efficiency of ab-initio total energy calculations for metals and semiconductors using a plane-wave basis set. *Comp. Mater. Sci.* **1996**, *6*, 15–50. [[CrossRef](#)]
27. Blochl, P.E. Projector augmented-wave method. *Phys. Rev. B* **1994**, *50*, 17953–17979. [[CrossRef](#)]
28. Perdew, J.P.; Burke, K.; Ernzerhof, M. Generalized gradient approximation made simple. *Phys. Rev. Lett.* **1997**, *78*, 1396. [[CrossRef](#)]
29. Dudarev, S.L.; Botton, G.A.; Savrasov, S.Y.; Humphreys, C.J.; Sutton, A.P. Electron-energy-loss spectra and the structural stability of nickel oxide: An LSDA+U study. *Phys. Rev. B* **1998**, *57*, 1505–1509. [[CrossRef](#)]
30. Yu, M.; Trinkle, D.R. Accurate and efficient algorithm for Bader charge integration. *J. Chem. Phys.* **2011**, *134*, 064111. [[CrossRef](#)]
31. Binder, K.; Ceperley, D.M.; Hansen, J.-P.; Kalos, M.; Landau, D.; Levesque, D.; Mueller-Krumbhaar, H.; Stauffer, D.; Weis, J.-J. *Monte Carlo Methods in Statistical Physics*; Springer Science & Business Media: Berlin/Heidelberg, Germany, 2012; Volume 7, pp. 195–233.
32. Ushakov, A.V.; Kukusta, D.A.; Yaresko, A.N.; Khomskii, D.I. Magnetism of layered chromium sulfides MCrS_2 (M = Li, Na, K, Ag, and Au): A first-principles study. *Phys. Rev. B* **2013**, *87*, 014418. [[CrossRef](#)]
33. Yang, H.; Huang, Z.; Jia, T.; Zhang, X.; Zeng, Z. Magnetic ordering and exchange striction stabilized geometric ferroelectricity in multiferroic AgCrS_2 . *J. Phys. Condens. Matter* **2016**, *28*, 236002. [[CrossRef](#)] [[PubMed](#)]
34. Streltsov, S.V.; Poteryaev, A.I.; Rubtsov, A.N. Magnetostriction and ferroelectric state in AgCrS_2 . *J. Phys. Condens. Matter* **2015**, *27*, 165601. [[CrossRef](#)] [[PubMed](#)]

35. Damay, F.; Petit, S.; Braendlein, M.; Rols, S.; Ollivier, J.; Martin, C.; Maignan, A. Spin dynamics in the unconventional multiferroic AgCrS_2 . *Phys. Rev. B* **2013**, *87*, 134413. [[CrossRef](#)]
36. Goodenough, J.B. Theory of the role of covalence in the perovskite-type manganites $[\text{La},\text{M}(\text{II})]\text{MnO}_3$. *Phys. Rev.* **1955**, *100*, 564–573. [[CrossRef](#)]
37. Kanamori, J. Superexchange interaction and symmetry properties of electron orbitals. *J. Phys. Chem. Solids* **1959**, *10*, 87–98. [[CrossRef](#)]
38. Anderson, P.W. Theory of magnetic exchange interactions: Exchange in insulators and semiconductors. *Solid State Phys.* **1963**, *14*, 99–214.
39. Landau, D.; Binder, K. *A Guide to Monte Carlo Simulations in Statistical Physics*, 5th ed.; Cambridge University Press: Cambridge, UK, 2021; pp. 7–49.
40. Erkişi, A. Ab Initio study on electronic and elastic properties of AgCr_2S_4 . *Acta Phys. Pol. A* **2021**, *140*, 243–251. [[CrossRef](#)]
41. Wang, V.; Xu, N.; Liu, J.-C.; Tang, G.; Geng, W.-T. Vaspkit: A user-friendly interface facilitating high-throughput computing and analysis using vasp code. *Comput. Phys. Commun.* **2021**, *267*, 108033. [[CrossRef](#)]
42. Maździarz, M. Comment on ‘the computational 2D materials database: High-throughput modeling and discovery of atomically thin crystals’. *2D Mater.* **2019**, *6*, 048001. [[CrossRef](#)]
43. Born, M.; Huang, K. *Dynamical Theory of Crystal Lattices*; Oxford University Press: New York, NY, USA, 1954; pp. 120–154.
44. Li, R.; Shao, Q.; Gao, E.; Liu, Z. Elastic anisotropy measure for two-dimensional crystals. *Extreme Mech. Lett.* **2020**, *34*, 100615. [[CrossRef](#)]
45. Falin, A.; Cai, Q.; Santos, E.J.; Scullion, D.; Qian, D.; Zhang, R.; Yang, Z.; Huang, S.; Watanabe, K.; Taniguchi, T. Mechanical properties of atomically thin boron nitride and the role of interlayer interactions. *Nat. Commun.* **2017**, *8*, 15815. [[CrossRef](#)] [[PubMed](#)]

Disclaimer/Publisher’s Note: The statements, opinions and data contained in all publications are solely those of the individual author(s) and contributor(s) and not of MDPI and/or the editor(s). MDPI and/or the editor(s) disclaim responsibility for any injury to people or property resulting from any ideas, methods, instructions or products referred to in the content.